



## MODELING AND SIMULATION OF HgCdTe BASED PHOTODETECTOR FOR N<sub>2</sub>O GAS DETECTION

<sup>1</sup>T. K. Parashar, <sup>2</sup>R. K. Lal

<sup>1</sup>University Polytechnic, <sup>2</sup>Department of Electronics and Communication Engineering  
Birla Institute of Technology, MESRA, Ranchi. [parashar303017@rediffmail.com](mailto:parashar303017@rediffmail.com)

Received 3/09/2011, online 16/09/2011

### Abstract

In this work an analytical modeling of p<sup>+</sup>-Hg<sub>0.81</sub>Cd<sub>0.19</sub>Te/n<sup>0</sup>-Hg<sub>0.81</sub>Cd<sub>0.19</sub>Te/CdZnTe, homojunction photodetector has been analyzed theoretically at 77K. A generic model of HgCdTe based photovoltaic detector has been developed using the closed form equations. Device parameters are obtained of the proposed photodetector and studied in terms of dark current, resistance area-product, quantum efficiency and detectivity. Study reveal that at suitable biasing conditions, the photodetector exhibits a high detectivity ( $2.6 \times 10^9$  mHz<sup>1/2</sup>/W) and suitable efficiency lies in wavelength range 15.5-19 μm with its peak at 17 μm. Proposed photodetector is best suited for N<sub>2</sub>O gas detection whose characteristic wavelength is 17 μm.

**Key words:** Photodetector; Gas; Modeling.

### I INTRODUCTION

The ternary alloy Hg<sub>1-x</sub>Cd<sub>x</sub>Te has become an important candidate for optoelectronic devices and optical gas sensor applications due to its broad band-gap range, better stability and has a weak dependence of the energy gap bandwidth on composition. No single known material surpasses MCT in fundamental performance and flexibility. Photovoltaic detectors fabricated from HgCdTe offer fast response times, higher sensitivity and/or higher operating temperatures over other infrared detectors [1-2]. Over the past few years, there has been tremendous progress in the development of HgCdTe based infrared photovoltaic detectors due to growing demand for both civilian (earth observation, environment sensing and monitoring) and military (target discrimination and identification, background clutter rejection) applications [3-4]. Mercury Cadmium Telluride (MCT) detectors have been the most important semiconductor for mid to very long-wavelength (3-

30 μm) infrared photodetectors. One major of utilization of these detector are in gas sensors in infrared region. A number of pollutant combustible/toxic gases and liquids such as hydrocarbons, Ammonia, Sulfur Dioxide, Nitrogen Dioxide, Nitric Oxide, Carbon Monoxide, Hydrogen Sulfide, Hydrogen Cyanide, Hydrogen Chloride, Chlorine, Arsine, Chlorine Dioxide, Fluorine, Hydrogen, Hydrogen Fluoride etc. having their characteristic absorption band located in the infrared region [5-6].

One basic drawback of these HgCdTe based devices are that they need to be operated in 77K temperature. But in compared to the ease of developed processing technology and remarkable performance obtained, it can be ignored. Here in this paper we have utilised the feature of HgCdTe based detector for the detection of N<sub>2</sub>O gas.

In present paper, an analytical model has been developed as generally used by many researchers

of this field for modeling of infrared photo detectors [7-11].

Therefore, an analytical model for a homojunction photodetector p+-Hg<sub>0.81</sub>Cd<sub>0.19</sub>Te/n-Hg<sub>0.81</sub>Cd<sub>0.19</sub>Te /CdZnTe with CdZnTe as substrate layer has been developed to explore the potential of the device for N<sub>2</sub>O detection. According to the researchers the characteristic wavelength of N<sub>2</sub>O gas is 17 μm

## II STRUCTURE

The proposed p<sup>+</sup>n homojunction photodetector structure and a diagram, showing the different mechanisms [diffusion, generation recombination and tunneling (BTB and TAT)] responsible for dark current, are shown in Fig.1. Structure consists of highly doped p+-Hg<sub>0.81</sub>Cd<sub>0.19</sub>Te over lightly doped n-Hg<sub>0.81</sub>Cd<sub>0.19</sub>Te which is virtually grown on a suitable substrate such as CdZnTe. The light has been assumed to be incident on the top p+- Hg<sub>0.81</sub>Cd<sub>0.19</sub>Te side of the photodetector to collect large quantity of illumination.

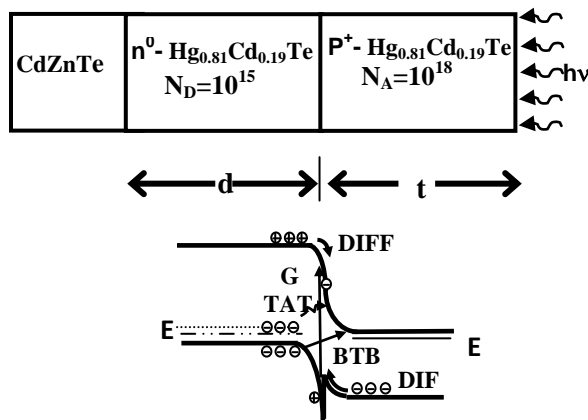


Fig.1 Schematic structure of the proposed photodetector and different dark current components

The incident light is absorbed in p+-Hg<sub>0.81</sub>Cd<sub>0.19</sub>Te and n-Hg<sub>0.81</sub>Cd<sub>0.19</sub>Te regions. The HgCdTe based p+n photodiode for long wavelength has been modeled and simulated. The uniform doping has been assumed for all neutral regions in simulation.

For the simulation of dark current, all associated AUGER, SRH (shockley–Read–Hall) and OPTICAL (band-to-band) recombination mechanisms models have been taken into account. Standard tunneling model has been considered for tunneling mechanism which consist total tunnelling current, I<sub>tot</sub> arising both possible tunnelling components due to (a) band to band tunnelling (I<sub>bb</sub>) as well as (b) trap assisted tunnelling (I<sub>ta</sub>). The surface recombination process at the contacts has been taken into account in modeling. We have taken into account the Fermi-Dirac statistics for parabolic shape of conduction band in all the calculations.

## III. ANALYTICAL MODELING

### III. 1 Dark Current

The major components of dark current in p<sup>+</sup>-n<sup>0</sup>-Hg<sub>0.81</sub>Cd<sub>0.19</sub>Te homojunction PIN-photodetector include (i) the diffusion of the thermally generated carriers from the neutral regions, I<sub>DIFF</sub> (ii) generation-recombination of carriers in the depletion region, I<sub>GR</sub> (iii) tunneling of carriers through the barrier, I<sub>TUN</sub> In order to generalize the analysis, we have however considered both trap assisted tunneling (TAT) as well as band-to-band tunneling (BTB).The tunneling component of current thus constitutes two components e.g., I<sub>TAT</sub> arising from the trap assisted tunneling and I<sub>BTB</sub> arising out of band-to-band tunneling. The net the top p+ layer receives the incident light through CdZnTe substrate, which is transparent to incident light, and the lightly doped n0 region acts as the active layer. The incident light is absorbed in the neutral p+, n0 regions as well as in the space charge region formed at the p+-n0 junction. The interfacial surface recombination due to non-ideal passivation conditions has also been considered in

present model. The magnitude of total dark current [12] of the photodetector is

$$I_{net} = I_{diff} + I_{gr} + I_{tat} + I_{btb} \quad [1]$$

### III. 2 Diffusion Current

In the present structure under consideration, the diffusion of minority carriers from both p+ and n regions, contribute diffusion current. The minority carrier diffusion current under application of a bias voltage, V can be obtained by solving 1-D diffusion equation under appropriate boundary conditions. Diffusion current density due to holes injected from p+ region in n- Hg<sub>0.81</sub>Cd<sub>0.19</sub>Te region is modeled as [12]

$$J_{diff} = qn_i^2 \sqrt{\frac{KT}{q}} \left( \sqrt{\frac{\mu_n}{\tau_n}} \cdot \frac{1}{N_a} + \sqrt{\frac{\mu_p}{\tau_p}} \cdot \frac{1}{N_d} \right) \left( \exp\left(\frac{qV_d}{KT}\right) - 1 \right) \quad [2]$$

In the above equations,  $n_i$  is the intrinsic carrier concentration of HgCdTe,  $N_a$  and  $N_d$  are the acceptor and donor concentrations in p and n regions respectively,  $q$  is the electronic charge,  $\mu_n$  and  $\mu_p$  are the hole and electron mobility respectively,  $\tau_n$  and  $\tau_p$  are hole and electron life times respectively .

The product of dynamic resistance and area (ROA) is given by the reciprocal of the derivative of the current density with respect to the voltage. The diffusion component of ROA product can be obtained as

$$\frac{1}{(ROA)_{diff}} = \frac{dJ_{diff}}{dV} \quad [3]$$

### III. 3 Generation-Recombination Current

The generation-recombination current component [12] arises due to impurities and defects within the depletion region that acts as intermediate

states for the thermal generation and recombination of carriers. These intermediate states are known as Shockley-Read-Hall centers. This current could be important than diffusion current, although depletion region is much less than the minority carriers diffusion length, especially at low temperature. The generation-recombination component of current density and associated resistance area product can be approximated as in

$$J_{gr} = \frac{n_{iW_0} KT}{\tau_0 V_{bi}} \cdot \frac{2 \sinh\left(\frac{qV_d}{2KT}\right)}{\left(1 - \frac{V_d}{V_{bi}}\right)} \cdot f(b) \quad [4]$$

### III. 4 Trap-assisted tunneling current

Trap-assisted tunneling occurs when minority carriers tunnel from occupied trap states on quasi neutral side to the empty band states on the other side of the junction or through trap sites present in the depletion region of the junction. These trap centers are intermediate energy levels created by the presence of impurities in the material. The trap-assisted tunneling component of current [12] calculated on the basis of simple one dimensional model and resistance area product associated with trap assisted tunneling can be written as in eqn 5.

$$J_{TAT} = \frac{\pi^2 q^2 N_t m_e^* M^2 (V_{bi} - V_d)}{h^3 (E_g - E_t)} \exp\left(-\frac{\sqrt{3} E_g^2 F(a)}{8\sqrt{2} qpE}\right) \quad [5]$$

### III. 5 Band-to-band tunneling current

When the crossover of energy bands take place at high reverse bias voltage, the band to band tunneling current arises due to flow of electrons from fully occupied valance band of p-region to partially filled or empty states of conduction band of n-region. Band-to-band tunneling current can be written as [12]

$$J_{BBT} = \frac{q^3 \sqrt{2m_e^*} E(V_{bi} - V_d)}{4\pi^2 \hbar^2} \exp\left(-\frac{\pi \sqrt{\frac{m_e^*}{2E_g^{3/2}}}}{2qEh}\right) \quad [6]$$

The band to band tunneling current and band-to-band tunneling component of  $R_0A$  product can be obtained as [9]. Considering the effect of all the two mechanisms discussed above, the net value of the resistance area product can be written as

$$\frac{1}{R_0A_{net}} = \frac{1}{R_0A_{diff}} + \frac{1}{R_0A_{gr}} + \frac{1}{R_0A_{lat}} + \frac{1}{R_0A_{btb}} \quad [7]$$

### III. 6 MODELING OF CARRIER LIFETIME

In order to compute the drift and diffusion components of current accurately, it is necessary to model the lifetime of minority carriers considering all the possible recombination mechanisms. In the present lifetime modeling, we have considered bulk recombination processes in HgCdTe to involve radiative recombination and two non-radiative recombination mechanisms. The direct band-to-band photon assisted recombination is radiative recombination and the phonon assisted recombination processes consists of Auger and Shockley-Read-Hall (SRH) recombination mechanisms which are non-radiative recombination processes. The modeling of the radiative recombination process is straightforward. For direct bandgap HgCdTe semiconductors, the lifetime of carriers due to radiative recombination for low level injection can be approximated as in [13-14].

The non-radiative Auger recombination is quite complex. It is an important mechanism in determining the performance of light-emitting devices and infrared detectors made from narrow-gap semiconductors. A semiconductor with a single conduction band and heavy-hole and light-

hole valence band there can be at least ten different types of Auger transitions occur. Out of these transitions, the two most significant transitions that occur at the minimum threshold energy ( $E_T \approx E_g$ ) are the Auger-1 or CHCC (involving two conduction band electrons and a heavy hole) and Auger-7 or CHLH (involving one conduction band electron and one heavy hole and one light hole). The former is generally dominant in n-type material and the later in p-type material. The net Auger recombination lifetime of the carriers can thus be written as in [15]. The Auger-1 recombination process involves the direct band-to-band recombination of a conduction band electron with a heavy hole and excitation of another electron in conduction band, dominant in n-type HgCdTe material. The details of computation of the various components of Auger recombination lifetime is discussed in details elsewhere [16]. The net lifetime of excess carriers in HgCdTe may be written as

$$\frac{1}{\tau_{eff}} = \frac{1}{\tau_R} + \frac{1}{\tau_{SRH}} + \frac{1}{\tau_{AU}} + \frac{2S}{d} \quad [8]$$

Where  $\tau_{AU}$  is the Auger lifetime,  $\tau_R$  is the radiative lifetime,  $\tau_{SRH}$  is the Shockley-Read-Hall lifetime,  $S$  is the surface recombination velocity, and  $d$  is the thickness of the HgCdTe epitaxial layer. This expression only takes into account surface recombination at the HgCdTe surface and substrate interfaces, where the surface recombination velocity is assumed to be equal to  $S$  at both interfaces

#### a. Radiative Lifetime

Radiative recombination is a direct band-to-band recombination of electrons from the conduction band with heavy holes in the valence band, as shown in Fig.1. Such a transition involves the

release of a photon in a direct bandgap semiconductor such as HgCdTe and is termed radiative recombination. An expression for the radiative lifetime is given by Schacham et al. as

$$\tau_R = \frac{n_i^2}{G_R(n_0 + p_0)} \quad [9]$$

where  $G_R$  is the spontaneous generation rate ( $s^{-1}$ )

$$G_R = n_i^2 5.8 \times 10^{-13} \epsilon_\infty^{1/2} \left( \frac{m_0}{m_e^* + m_v^*} \right)^{3/2} \left( 1 + \frac{m_0}{m_c^*} \right) \times \left( \frac{300}{T} \right)^{3/2} \left( E_g^2 + 3kTE_g + 3.75(kT)^2 \right) \quad [10]$$

$m_v^*$  and  $m_c^*$  are the effective masses of holes in the valence band and electrons in the conduction band, respectively,  $\epsilon_\infty$  is the high frequency relative permittivity,  $k$  is Boltzmann's constant in eV, and  $m_0$  is the rest mass of an electron.

### b. Shockley-Read-Hall (SRH) lifetime

When the periodicity of the crystal lattice in a semiconductor is interrupted by an impurity and crystal defect, energy levels may appear within the forbidden gap of the electronic band structure. These energy levels, or traps, increase the probability of electron transitions between the conduction and valence bands, thus reducing the net lifetime of excess carriers in the semiconductor.

In SRH recombination process an electron in the conduction band is captured by a SRH center within the bandgap, and later emitted by the center to the valence band, wherein it recombines with a hole. The position of the SRH centers within the forbidden gap is given by  $E_t$ , being the energy of the centers above the valence band edge at  $E_v = 0$ . The expression used to describe the SRH lifetime is

$$\frac{1}{\tau_{SRH}} = \frac{(n_0 + n_1)\tau_{p0} + (p_0 + p_1)\tau_{n0}}{n_0 + p_0} \quad [11]$$

$$\tau_{p0} = \frac{1}{C_p N_t} \quad \text{and} \quad \tau_{n0} = \frac{1}{C_n N_t} \quad [12]$$

where  $C_p$  and  $C_n$  are the capture coefficients for holes and electrons, respectively,  $N_t$  is the trap density, and  $n_0$  and  $p_0$  are the equilibrium concentrations of electrons and holes, respectively. Here,  $C_p$  is taken as  $3.0 \times 10^{-15} m^3 s^{-1}$ ,  $C_n$  is taken as  $1.9 \times 10^{-13} m^3 s^{-1}$ , and Assuming mercury vacancies are the primary SRH trap.  $n_1$  and  $p_1$  are the electron and hole density in the conduction band and valence respectively, when the Fermi level  $E_f$  is at the trap energy  $E_t$ . These densities are given by the following expressions,

$$p_1 = N_v \exp\left(-\frac{E_t}{kT}\right) \quad \text{and}$$

$$n_1 = N_c \exp\left(-\frac{(E_g - E_t)}{kT}\right) \quad [13]$$

$N_c$  and  $N_v$  are the density of states in the valence and conduction bands, respectively and are given by

$$N_v = 2 \left( \frac{2\pi m_h kT}{\hbar^2} \right)^{1.5} \times 10^{-6}$$

$$N_c = 2 \left( \frac{2\pi m_e kT}{\hbar^2} \right)^{1.5} \times 10^{-6} \quad [14]$$

### c. Auger Lifetime

In general, multi-carrier interactions which result in electron-hole recombination are termed Auger recombination. In n-type  $Hg_{1-x}Cd_xTe$  the Auger-1 process dominates, in which an electron in the conduction band recombines with a hole in the heavy-hole band, while at the same time another conduction band electron is promoted to a higher energy level in the conduction band.

The mean time between Auger-1 recombination events is given by

$$\tau_{A1} = \frac{2n_i^2}{(n_0 + p_0)n_0} \tau_{A1}^i \quad [15]$$

Where  $\tau_{A1}^i$  is the intrinsic lifetime for the Auger-1 process, given by

$$\tau_{A1}^i = 3.8 \times 10^{-18} \epsilon_{\infty}^2 \left( \frac{m_0}{m_c} \right) (1+\gamma)^{0.5} (1+2\gamma) \left( \frac{E_g}{kT} \right)^{3/2} \times \exp \left( \frac{(1+2\gamma)E_g}{(1+\gamma)kT} \right) |F_1 F_2|^{-2} \quad [16]$$

Where  $\gamma = (m_c/m_v)$ , and  $|F_1 F_2|$  is the overlap integral of the Bloch functions. The overlap integral is known to be  $0.1 < |F_1 F_2| < 0.3$ , however it cannot be determined accurately. For this work  $|F_1 F_2| = 0.2$  has been used.

$$\tau_{A7} = \gamma' \tau_{A1} \quad [17]$$

Recent direct measurements at 77K of carrier recombination show  $\gamma' = 8$  for  $x \approx 0.194$ .

### III.7 Quantum Efficiency

The quantum efficiency ( $\eta$ ) of a p-n junction photodetector has generally three major components. These components arise from the contribution of the three regions e.g., neutral n-region ( $\eta_n$ ), neutral The optical generation p-region ( $\eta_p$ ) and the depletion region ( $\eta_{dep}$ ). rate of electron-hole pairs, as a function of distance  $x$  from the surface can be written as [17-18]

$$\eta = \eta_n + \eta_p + \eta_{dep} \quad [18]$$

$$\eta_p = \frac{(1-r_p)\alpha_p L_n}{\alpha_p^2 L_n^2 - 1} \left[ \frac{\alpha_p L_n + \gamma_n - \exp\{-\alpha_p(t-x_p)\} \left[ \gamma_n \cosh\left(\frac{t-x_p}{L_n}\right) + \sinh\left(\frac{t-x_p}{L_n}\right) \right]}{\gamma_n \sinh\left(\frac{t-x_p}{L_n}\right) + \cosh\left(\frac{t-x_p}{L_n}\right)} - \alpha_p L_n \exp\{-\alpha_p(t-x_p)\} \right] \quad [19]$$

$$\eta_n = \frac{(1-r_p)(1-r_n)\alpha_n L_p}{\alpha_n^2 L_p^2 - 1} \exp\{-\alpha_p t + \alpha_n w_n\} \left[ \frac{(\gamma_p - \alpha_n L_p) \exp\{-\alpha_n(d-x_n)\} - \left[ \gamma_p \cosh\left(\frac{d-x_n}{L_p}\right) + \sinh\left(\frac{d-x_n}{L_p}\right) \right]}{\gamma_p \sinh\left(\frac{d-x_n}{L_p}\right) + \cosh\left(\frac{d-x_n}{L_p}\right)} + \alpha_n L_p \right] \quad [20]$$

$$\eta_{dep} = (1-r_n)(1-r_p) \left[ \exp(-\alpha_p(t-x_p)) - \exp(-(\alpha_p t + \alpha_n x_n)) \right] \quad [21]$$

the photo-generated carriers in the depletion region can be obtained as above equations

### III.8 Specific Detectivity

The most important figure of merit of the photodetector for use toxic gas monitoring is the specific detectivity  $D^*$ , which depends on the wavelength of incident light  $\lambda$ , the quantum efficiency  $\eta$  and zero bias resistance area product,  $ROA$ .

$$D^* = \frac{q\eta\lambda}{hc} \sqrt{\frac{RA_{net}}{4kT}} \quad [22]$$

As the dark current of the detector is contributed by three major components e.g., diffusion, generation-recombination and tunneling (which includes trap assisted tunneling (TAT) and band to band tunneling (BTB)), the detectivity of the photodetector under consideration should be estimated from the net value of  $ROA$  product arising out of these mechanism. The specific detectivity of the photodetector which is a function of the applied voltage can be written as [20-21]

### III.9 Responsivity

The responsivity ( $\mathfrak{R}$ ) of the photodetector depends on the wavelength of incident light  $\lambda$ , the quantum efficiency  $\eta$  [22-23]

The equation to obtain responsivity is given as

$$R = \frac{\eta q \lambda}{hc} \quad [23]$$

#### IV. RESULTS AND DISCUSSIONS

Numerical computations have been carried out on p+-Hg<sub>0.81</sub>Cd<sub>0.19</sub>Te / n-Hg<sub>0.81</sub>Cd<sub>0.19</sub>Te/ CdZnTe p<sup>+</sup>n homojunction photodetector at 77K for operation at LWIR. The light has been assumed to be incident on the top p+-Hg<sub>0.81</sub>Cd<sub>0.19</sub>Te side of the photodetector. The photons with energy higher than the energy gap create electron-hole pairs in p and n region. The band gap of Hg<sub>1-x</sub>Cd<sub>x</sub>Te as a function of temperature, T and alloy composition, x is included in the simulation model using the empirical formula as in table-1. The formula for

intrinsic carrier concentration [25-27] and value of hole mobility is also shown in table-1 [25]. Reported values of hole effective mass and electron effective mass based on computation by Kane band model are used and given in table-1 [26]. Absorption coefficient given as

$$\alpha = \alpha_0 \exp\left[\frac{\sigma(E - E_0)}{T + T_0}\right]$$

$$\sigma = 3.267 \times 10^4 (1 + x) \quad [24]$$

Where  $\alpha_0 = \exp(53.61x - 18.88)$ ,  $E_0 = -0.3424 + 1.838x + 0.148x^2$  (eV),  $T_0 = 81.9$  (K),  $\sigma = 3.267 \times 10^4(1 + x)$  (Kelvin/ eV) are fitting parameters which vary smoothly with composition.

TABLE I. DEVICE PARAMETER USED IN THE COMPUTATION

Parameter	Values
$N_D$ $N_A$	$10^{15} \text{ m}^{-3}$ $10^{18} \text{ m}^{-3}$
$N_f$	$10^{20} \text{ m}^{-3}$
Bandgap	$E_g = -0.302 + 1.93x + 5.35 \times 10^{-4} T(1 - 2x) - 0.810x^2 + 0.832$
t	$3 \mu\text{m}$
d	$1 \mu\text{m}$
Dielectric constant	$\epsilon_r = (15.15 + 1.65x) \epsilon_0$ $\epsilon_\infty = 15.2 - 15.6x + 8.2x^2$ $\epsilon_0 = 20.5 - 15.6x + 5.7x^2$ [27]
Electron effective mass $m_e^*$	$m_0 \exp\left[\frac{4}{3} \ln\left(\frac{n_i}{3.126 \times 10^{15} T^{3/2} \exp(-E_g / 2kT)}\right)\right]$
Hole Effective mass $m_h^*$	$0.55m_0$
Mobility of electron	$\mu_e = \frac{9 \times 10^8 s}{T^{2r}}$ where $r = \left(\frac{0.2}{x}\right)^{0.6}$ $s = \left(\frac{0.2}{x}\right)^{7.5}$
Mobility of hole	$\mu_h = \mu_0 \left[1 + \left(\frac{p}{1.8 \times 10^{17}}\right)^2\right]^{-1/4}$

The different components of the dark current and

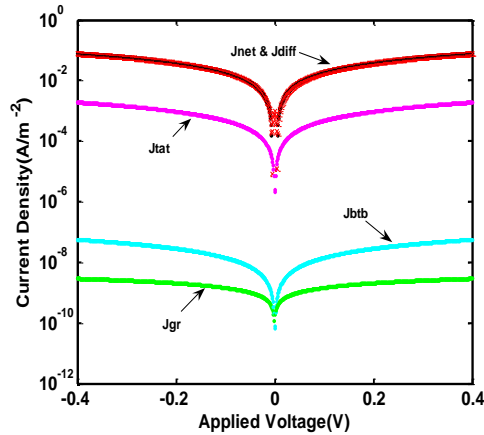


Fig.2. Current density and its components with applied voltage

the  $R_0A$  products have been calculated using our proposed theoretical model. In present work the variation of the  $R_0A$  product with applied voltage and as well as the major parameters of the gas detectors such as Detectivity and quantum efficiency on the applied wavelength has been estimated quantitatively. In Fig 2 shows the variation of the net dark current along with its component due to major three recombination mechanism diffusion, generation-recombination and tunnelling (BTB+TAT) with the applied bias voltage. Major current flows in the detector due to diffusion and tunnelling components. However net current density dominated by diffusion current. Due to their very small values the GR and BTB component of dark current could not affect the total dark current considerably.

In Fig 3, the variation of  $R_0A_{net}$  and its component for the  $e_t = 0.0474$  eV, [calculated by  $e_t = 0.7 \times E_g$  as suggested by different researchers and used in our modelling] is shown with applied voltage. As obvious, here we can observe that  $R_0A_{net}$  value depends mainly on the diffusion component and very small resistance (of the order of  $\sim 10^2 \Omega\cdot m^2$ )

is obtained.

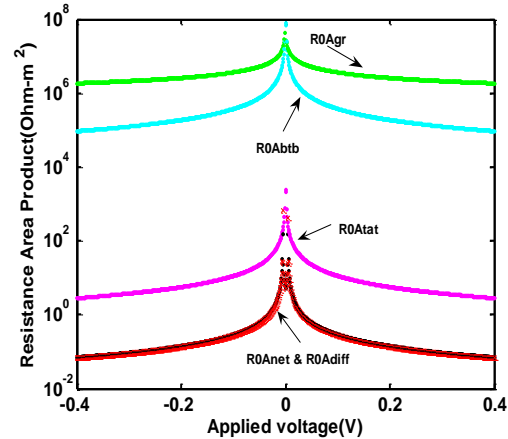


Fig.3.  $R_0A_{net}$  and its component with respect to applied voltage

The large tunnelling current density ( $\sim 10^{-2} \text{ A/m}^2$ ) due to Trap level also helps in reducing the detector resistance.

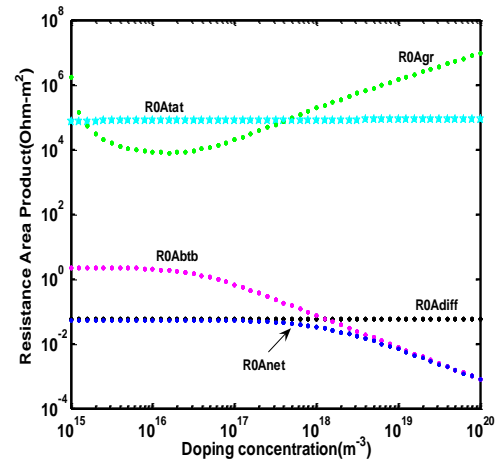


Fig.4.  $R_0A_{net}$  with respect to applied voltage at different  $N_D$

In Fig 4 shown below, the variation of  $R_0A_{net}$  and its component is plotted with an another important material parameter that is doping concentration in  $n^0$  region. Here we observed that only diffusion and Trap assisted tunnelling remain unaffected by increase in doping concentration. Other two Band to band tunnelling (which decreases almost

sharply) and GR (which increases rapidly) affected a lot by  $N_D$  variation on n-Hg<sub>0.81</sub>Cd<sub>0.19</sub>Te.

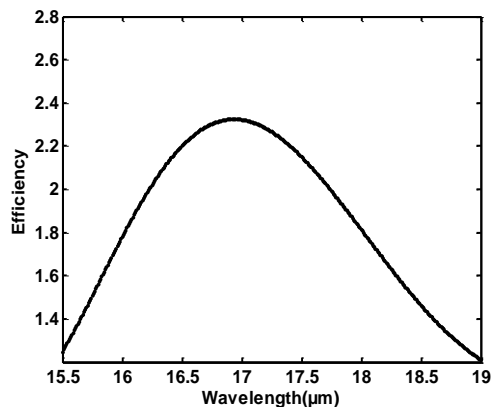


Fig.5. Efficiency with respect to operating wavelength. The quantum efficiency and specific device are the two main device parameter in terms of which the performance of the detector is described. Thus in Fig 5 variation of the efficiency of the detector with respect to operating wavelength has been presented. In present case, the efficiency of the detector achieves its maximum value  $\sim 2.4$  at  $17 \mu\text{m}$ . It decreases sharply on the both side. One can see that the efficiency is more than 1.5 between the wavelength ranges  $15.5 \mu\text{m}$  to  $18 \mu\text{m}$  which may be consider the range over which the device can be utilise as detector. For non telecommunication applications such as gas sensor device can be utilised as detector for  $N_2O$  gas whose characteristic wavelength is  $17\mu\text{m}$ .

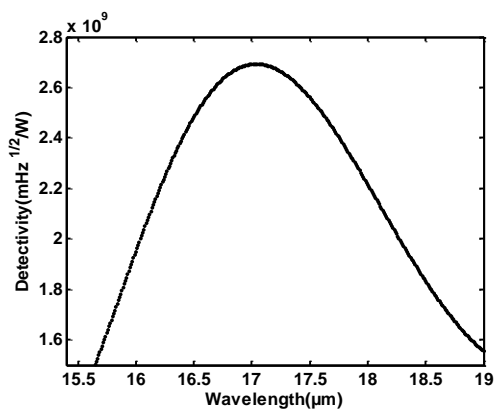


Fig. 6. Detectivity with respect to operating wavelength.

This fact is also supported by the variation of detectivity shown in figure 6. Here also the peak detectivity ( $\sim 2.7 \times 10^9 \text{ mHz}^{1/2}/\text{W}$ ) is obtained at  $17 \mu\text{m}$ . Signature wavelength of the nitrous oxide gas,  $N_2O$  is  $17 \mu\text{m}$  and its emissions are mainly determined by food supply, because these emissions largely stem from soil processes induced by agriculture. Like  $CH_4$ ,  $N_2O$  emissions are generally highest in the regional wealth scenario.  $N_2O$  emissions are generally affected by large uncertainties, because these are mainly caused by bacterial soil processes and are therefore difficult to measure. Extensive research into  $N_2O$  detectors are still a major required. The present work is a small contribution in this direction. On the basis of the result obtained from the present work we can say that this detector is best suited for  $N_2O$  gas detection.

### V. CONCLUSION

The performance of the device has been examined by self generated (our own developed ) MATLAB coded analytical model for photodetector to compute the dark current density, zero bias area product, quantum efficiency and detectivity. We got high efficiency maximum value  $\sim 2.4$  at  $17 \mu\text{m}$  and high detectivity  $D = 2.7 \times 10^9 \text{ mHz}^{1/2}/\text{W}$ . The present photodetector performs best in the wavelength range  $15.5 \mu\text{m}$  to  $18 \mu\text{m}$ . However, If used for the gas detection, it is best suited for detection of  $N_2O$  gas (Characteristic wavelength  $17\mu\text{m}$ ).  $N_2O$  detection is useful for agriculture related (mainly related with soil processing) applications.

### References

1. A Rogalski, J Antoszewski and L Faraone, "Third-generation infrared photodetector arrays," *J. Appl. Phys.* 105, 09110 (2009).
2. Chang Y, Grein C H, Zhao J, Becker C R, Flatte M E, Liao P K, Aqariden F and Sivananthan S. "Carrier recombination lifetime characterization of molecular beam epitaxially grown HgCdTe," *Appl. Phys. Lett.* **93**, 192111 (2008).
3. Le Perchec J, Y Desieres and Espiau de R Lamaestre, "Plasmon-based photosensors comprising a very thin semiconducting region," *J. Appl. Phys. Lett.* **94**, 181104 (2009).
4. A Zemel, I Lukomsky and J. E Weiss. "Mechanism of carrier transport across the junction of narrow band-gap planar n+p HgCdTe photodiodes grown by liquid-phase epitaxy," *J Appl.Phys.* **98**, 054504,(2005).
- 5..A. Rogalski, K. Adamiec and J. Rutkowski, "Narrow-Gap Semiconductor Photodiode", SPIE Press, Bellingham, USA, (2000).
6. A. Rogalski, "Third generation infrared detectors Proceedings of the Symposium on Photonics Technologies for 7th Framework Program, Wroclaw 12-14 October (2006).
7. M Mello, B Potil, A Risi, A de Passaseo, M Lomascolo and M. De Vittorio, "GaN optical system for CO and NO gas detection in the exhaust manifold of combustion engines," *J. Opt. A: Pure Appl. Opt.* **8**, S545–S549 (2006).
8. P. Chakrabarti, P.K. Saxena and R.K. Lal, "Analytical Simulation of an InAsSb photovoltaic detector for mid-infrared applications," *J. Infrared and Millimeter waves*, **27**, 1119, (2006).
9. R.K. Lal, M. Jain, S. Gupta and P.Chakrabarti, "An analytical model of a double-heterostructure mid-infrared photodetector" *Infrared Physics and Technology*, **44**, 125 (2003).
10. H. H. Gao, A. Krier and V. V. Sherstnev, "Room temperature InAs<sub>0.89</sub> Sb<sub>0.11</sub> photodetectors for CO detection at 4.6  $\mu\text{m}$ ", *Applied Phys. Lett.*, **77**, 872 (2000).
11. Mello, M., Potil, B, Risi, A de Passaseo, A, Lomascolo M. and Vittorio, M. De, "GaN optical system for CO and NO gas detection in the exhaust manifold of combustion engines," *J. Opt. A: Pure Appl. Opt.* **8**, S545–S549 (2006).
12. Hu, W.D. Chen, X.S. Quan, Z.J. Li, Z.F. Liao, Q.J. Ye, Z.H. Hu, X.N. Lu, W, "Simulation and design consideration of photoresponse for HgCdTe infrared photodiodes," *Shanghai Inst. of Tech. Phys., Chinese Acad. of Sci., Shanghai*, **39** (2008).
13. V.C.Lopes, A.J.Syllaios and M.C.Chen, "Minority carrier lifetime in mercury cadmium telluride," *Semicond. Sci. Technol.*, **8**, 824 (1993).
14. S.H.Shin, J.M.Arias, M. Zandian, J.G.Pasko and R.E.DeWames, "Effect of the dislocation density on minority-carrier lifetime in molecular beam epitaxial HgCdTe," *Appl. Phys. Lett.* , **59**, 21 (1991).
15. .S. Krishnamurthy and T.N. Casselman, "A Detailed Calculation of the Auger Lifetime in p-Type HgCdTe," *Journal of Electronic Materials*, 29 (6), 828 (2000).

- 16 M A Kinch Fundamental physics of infrared detector materials J. Electron. Mater. **29**, 809 (2000).
17. Y. Tian, B. Zhang, T. Zhan, H. Jiang, and Y. Jin, "Theoretical analysis of the detectivity in N-p and P-n GaSb/GaInAsSb infrared photo-detectors," IEEE Trans. Electron Dev., vol. **ED-47**, 544 (2000).
18. P. Chakrabarti, A. Krier, and A. F. Morgan, "Analysis and simulation of a mid-infrared P+-InAs<sub>0.55</sub>Sb<sub>0.15</sub>P<sub>0.30</sub>/n-InAs<sub>0.89</sub>Sb<sub>0.11</sub>/N+-InAs<sub>0.55</sub>Sb<sub>0.15</sub>P<sub>0.30</sub> double heterojunction photodetector grown by LPE," IEEE Trans. Electron Devices, **50**, 2049 (2003).
19. A. D. D. Dwivedi, "analytical modeling and atlas simulation of p+-Hg<sub>0.78</sub>Cd<sub>0.22</sub>Te/n-Hg<sub>0.78</sub>Cd<sub>0.22</sub>Te/CdZnTe homojunction photodetector for lwir free space optical communication system," journal of electron devices, **9**, 396 (2011).
20. A.D.D. Dwivedi, Arun Kumar Singh, Rajiv Prakash and P. Chakrabarti, "A Proposed Organic Schottky Barrier Photodetector for application in the Visible Region," Current Applied Physics, **10**, 900 (2010).
21. Arun Kumar Singh, A. D. D. Dwivedi, P. Chakrabarti and Rajiv Prakash, "Electronic and Optical Properties of Electrochemically Polymerized Polycarbazole/Aluminum Schottky Diodes," Journal of Applied Physics, **105**, 114506 (2009).
22. Yi Gong, T Yamaguchi, H Kan, T Makino, T Iida, T Kato, M. Aoyama, Y. Hayakawa and M Kumagawa, "Room-Temperature Mid-Infrared Light-Emitting Diodes from Liquid-Phase Epitaxial InAs/InAs<sub>0.89</sub>Sb<sub>0.11</sub>/InAs<sub>0.80</sub>P<sub>0.12</sub>Sb<sub>0.08</sub> Heterostructures," J. Appl. Phys. **362614**, (1997).
23. J.V.Gumenjuk-Sichevskaya and F.F.Sizov, "Currents in narrow-gap photodiodes," Semicond. Sci. Technol, **14**, 1124 (1999).
24. G L Hansen and J L Schmit, "Calculation of intrinsic carrier concentration in Hg<sub>1-x</sub>Cd<sub>x</sub>Te J. Appl. Phys. **54**, 1639 (1983).
25. M.H. Weiler, "Magneto-optical properties of Hg<sub>1-x</sub>Cd<sub>x</sub>Te Alloyed," in Semiconductors and Semimetals, edited by R.K. Willardson And A.C. Beer, Academic Press, New York **16**, 119 (1981).
26. J P Rosbeck, R E Star, S L Price and K J Riley, "Background and temperature dependent current-voltage characteristics of Hg<sub>1-x</sub>Cd<sub>x</sub>Te photodiodes," J. Appl. Phys. **53**, 6430 (1982).
27. P N J Dennis, C T Elliott and C L Jones, "A method for routine characterization of the hole concentration in p-type cadmium mercury telluride," J. Infrared Phys. **22**, 167 (1982).